Proceedings of ES2008
Energy Sustainability 2008
August 10-14, 2008, Jacksonville, Florida USA

ES2008-54098

STUDY OF A QUENCH DEVICE FOR SYNTHESIS AND HYDROLYSIS of Zn NANOPARTICLES: MODELING AND EXPERIMENTS

Aiman Alshare, Tareq Abu Hamed, Marc Brülhart[1], Luke Venstrom, and Jane H. Davidson

Department of Mechanical Engineering, University of Minnesota, Minneapolis, MN 55455, USA

ABSTRACT

The synthesis and hydrolysis of zinc nanoparticles are carried out in a tubular reactor. A key component of the reactor is a coaxial jet quench device. Three co-axial and multi-inlet confined jets mix Zn(g), steam and argon to produce and hydrolyze zinc nanoparticles. The performance of the quench device is assessed with computational fluid dynamic modeling and measurements of hydrogen conversion and particle size and composition. Numerical data elucidate the impact of varying jet flow rates on temperature and velocity distributions within the reactor. Experiments produce hydrogen conversions of 61 to 79 %. Particle deposition on sections of the reactor surface above 650 K favors hydrolysis. Residence time for in-flight particles is less than one second and these particles are partially hydrolyzed.

1. INTRODUCTION

A process to produce hydrogen without the use of fossil fuel is solar thermochemical water splitting via a two-step metal redox cycle. The zinc-zinc oxide pair is most suitable for this cycle because zinc oxide dissociates at temperatures attainable in concentrating solar reactors [1-7]. In the first, solar step of the cycle, zinc oxide spontaneously dissociates to zinc and oxygen at 2335 K:

$$ZnO \Leftrightarrow Zn + 1/2\, O_2 \qquad \Delta H_{298K} = 351 \text{ kJ/mol} \qquad (1)$$

The second, non solar step is the exothermic hydrolysis of zinc yielding hydrogen and zinc oxide:

$$Zn + H_2O \Leftrightarrow ZnO + H_2 \qquad \Delta H_{298K} = -130 \text{ kJ/mol} \qquad (2)$$

The Gibbs free energy of reaction (2) at 650 K, which is the temperature of interest in the present study, is -128 kJ/mol, indicating negligible reverse reaction. The ZnO produced in the second step is recycled to the first step, completing the thermochemical cycle.

The present study focuses on the second, hydrolysis step. Ideally, all of the zinc reactant would be converted to hydrogen and zinc oxide and these products would be recovered continuously. In that respect, researchers have considered hydrolysis of Zn aerosol nanoparticles [8-15]. The hypothesis is that the large surface to volume ratio of nanoparticles will promote rapid hydrolysis and that an aerosol will permit continuous collection of the ZnO product.

In initial experiments conducted at the Swiss Federal Institute of Technology ETH-Zurich, evaporation of Zn was followed by in-situ hydrolysis with steam in an argon carrier gas [8,9]. Hydrogen conversion was as high as 72 % at an evaporation temperature of 1023 K. Hydrogen production was attributed to hydrolysis of Zn on the reactor walls and on a stainless steel rod that extended axially along the center of the reactor. Near the reactor inlet, where temperatures were above the saturation temperature of Zn, the authors suggest ZnO was formed by heterogeneous reaction of Zn(g) and steam on the reactor surfaces. At downstream positions where the reactor temperature was below the saturation temperature of Zn, both ZnO and Zn particles were present on the reactor surfaces. The authors infer from the morphology of the deposit that heterogeneous hydrolysis of Zn particles followed their deposition. Particles collected on a glass fiber filter positioned at the reactor exit were pure Zn. The mass of particles on the filter was not reported.

Similar experiments in a hot wall tubular reactor were performed at the University of Minnesota [10]. The influences of the reactor residence time and surface temperature on hydrogen conversion was measured for evaporation temperatures of 1023 and 1073 K. The hydrogen conversion was 88 and 96 % for temperatures above Zn saturation and residence times of 1.7 and 2.1 s, respectively. The presence and adhesion of ZnO on the quartz reactor surface suggests a probable mechanism for hydrolysis is heterogeneous reaction of Zn(g) and steam, similar to the findings of ETH [8,9].

Later experiments at the University of Minnesota were the first to obtain in-situ measurement of the size distribution and concentration of aerosol nanoparticles at temperatures below

[1] *Visiting graduate student researcher from the Swiss Federal Institute of Technology ETH-Zurich*

the Zn saturation temperature [11]. Particle concentration was greater than 700,000 particles/cm^3. The particle size distribution peaked at 28 nm. Hydrogen conversions were 51 to 56 %. Hydrogen production was attributed to hydrolysis of Zn nanoparticles in the carrier gas stream and particles on the reactor wall. Particles scraped from the wall of the reactor were 62 % ZnO or greater above 648 K. Below 648 K, the ZnO content was about 30 %.

Ernst *et al.* [12,13] studied Zn hydrolysis in a reactor divided into evaporation, condensation, and hydrolysis zones. They also observed that the conversion of zinc to hydrogen decreased with decreasing reactor temperature, and that hydrolysis occurred primarily by reaction of nanoparticles at the reactor wall. At 573 K, H_2 conversion was 60 % and that attributable to in-flight particles was 13 %. At 850 K, H_2 conversion was 90 % and the maximum conversion attributable to the aerosol was 17 %. Piatkowski [14] attempted to improve the nanoparticle synthesis process by using a fast quench rate on the order of 10^6 K/s. He measured hydrogen conversions between 56 and 76 %. Roughly 10 % of the Zn reactant was recovered as ZnO at a filter located outside the hot reaction zone. Most of the particles were deposited and hydrolyzed within the narrow passages of the quench device.

Funke *et al.* [15] studied the hydrolysis of Zn by feeding 158 nm Zn particles into a flow tube reactor at temperatures between 653 and 813 K, rather than forming particles in-situ. The highest hydrogen conversion observed was 24 % at 813 K for a gas residence time of 0.6 s. Most of the particles deposited on the walls of the reactor. Only 10 to 30 % of the Zn nanoparticles were collected from the gas stream on a filter. Furthermore, the particles collected on the filter were only partially hydrolyzed, while the particles on the reactor walls were completely hydrolyzed. Using non-isothermal thermogravimetric analysis (TGA), they measured an activation energy for Zn nanoparticle hydrolysis of 132 ± 27 kJ/mol. In comparison, Ernst [12] reports an activation energy of 43 ± 7 kJ/mol for 164 nm particles.

This paper presents data obtained in a second generation tubular reactor built at the University of Minnesota. The key new component of the reactor is a coaxial jet quencher that is referred to as the "quench ring." The device rapidly quenches Zn(g) with a mixture of steam and argon to form an aerosol of zinc and, due to simultaneous reaction, zinc oxide nanoparticles. The ring was originally conceived to increase the rate at which Zn(g) is cooled to below the saturation temperature and to minimize particle deposition on the wall of the reactor. The performance of the quench ring is assessed using computational fluid dynamics and experiments conducted at varying jet flow rates. Measurements include hydrogen conversion and analysis of the size and chemical composition of particles.

2. REACTOR DESIGN

Figure 1 is a sketch (not-to-scale) of the reactor and instrumentation. The reactor is divided into four sections: an evaporation section within an electric furnace ($x \leq 27$ cm), the quench ring ($27 \leq x \leq 28$ cm), a reaction section ($28 \leq x \leq 48$ cm), and a cooler collection section ($48 \leq x \leq 65$ cm).

The reactor consists of inner and outer quartz tubes. The outer quartz tube is 2.0 cm i.d. It is held in a concentric cylindrical electric furnace (Thermolyne 97500) with two insulated mounts. The second mount is positioned just downstream of the quench ring between x = 28 and 38 cm and is labeled as insulation in Fig. 1. Outside the furnace ($38 \leq x \leq 48$ cm), the quartz tube is wrapped with an electrical tape heater to maintain the reaction section at temperatures favorable to hydrolysis, 630 to 700 K. At x = 48 cm where the cooler collection section begins, the 2.0 i.d. quartz tube is connected to a 2.2 cm i.d. stainless steel tube. A glass fiber filter at x = 65 cm captures effluent particles. Hydrolysis in the collection section and on the filter is negligible.

The inner quartz tube houses a cylindrical crucible (at x = 0 cm) containing zinc pellets, and sits within the evaporation section inside the outer quartz tube. The inner tube is 1.5 cm i.d. at the crucible and tapers to 0.4 cm where it terminates at the quench ring.

A crucial component of the reactor is the quench ring. A rapid quench results in the synthesis of particles with large specific surface area [16], and as was discussed in the introduction, it is thought that large specific surface area enhances the rate of hydrolysis. To achieve rapid cooling rates, the quench ring uses three co-axial and multi-inlet jets, as shown in Fig. 2. Similar configurations are used in micro-can combustors to obtain a combustible mixture at short spatial scale. Jet flow rate ratios play a major role in controlling mixing [17,18]. The quench ring is constructed of two concentric stainless steel rings welded together. Each ring is machined to provide concentric rings of 1 mm holes through which steam and argon flow. The evaporated zinc gas and argon enter upstream and flow through a 4 mm diameter inlet at the center of the rings. Steam mixed with Ar is fed to the inner ring from a 0.12 cm i.d. stainless steel tube on the downstream side of the assembly. Steam is generated by an electrical heater fed with deionized water. The flow rate of steam is 0.8 ml/min. The inlet port for the H_2O/Ar feed tube is at x = 56 cm. Additional argon flows through the outer ring, again fed by a stainless steel tube on the downstream side of the assembly. The inlet port to the tube is at x = 59 cm.

Gas and wall temperature distributions in the reactor are measured using Chromel-Alumel (K-type) thermocouples. Flow rates are controlled and measured independently using mass flow meters. The mass flow meters are calibrated with a Gilibrator 2 calibration system (Sensidyne Inc) with an accuracy of ± 1 % l/min. The composition of the effluent gas is sampled using an inline gas chromatograph (GC, Agilent 6890). Water vapor is removed prior to sampling with a condenser and molecular sieve. A nanoscale Scanning Mobility Particle Sizer (SMPS) measures the size and number concentration of nanoparticles in the gas stream.

3. METHOD

3.1 Numerical model

The objective of the numerical modeling is to understand how the operating conditions for the quench ring

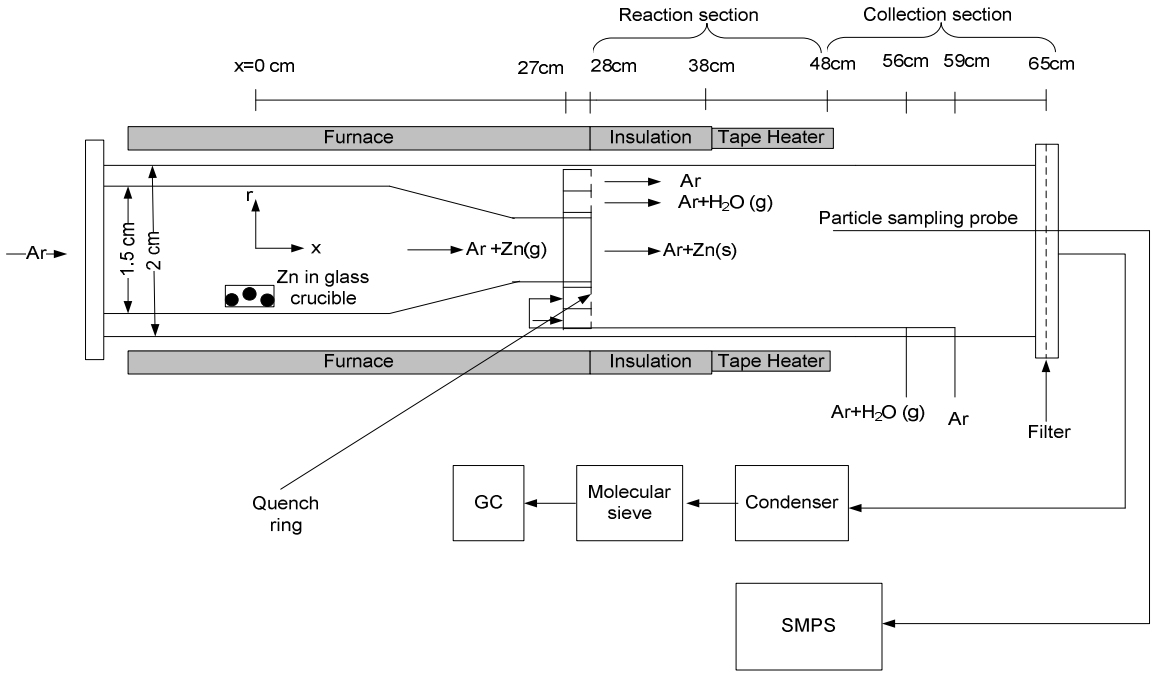

FIG. 1 EXPERIMENTAL APPARATUS

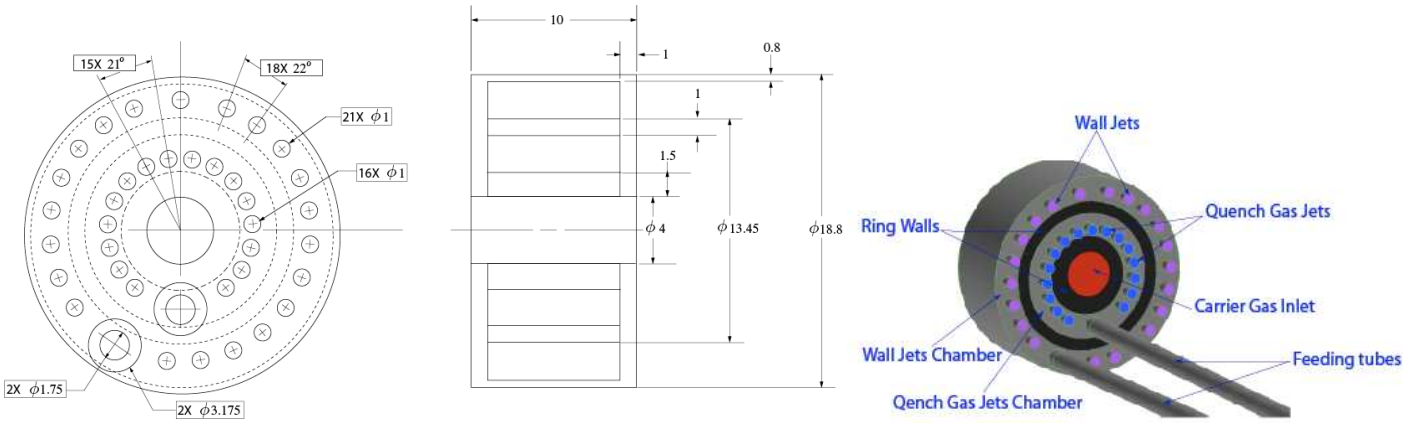

FIG. 2 QUENCH RING GEOMETRY (DIMENSIONS ARE mm)

affect the flow and temperature fields in the reactor and the quench rate of the gaseous zinc. Table 1 lists the operating conditions of the three numerical and experimental cases. Note that all cases have a center flow of Zn(g)/Ar equal to 0.75 l/min, and that the major difference in the cases is the relative flow rates of the H_2O/Ar and Ar jets. Furthermore, note that case 1 and 3 each have a total gas flow rate of 7.87 l/min, while case 2 has a lower total gas flow rate of 5.01 l/min.

The reactor is modeled from the upstream side of the quench ring at x = 27 cm to the exit of the reaction section at x = 65 cm. Three-dimensional, laminar incompressible models are applied to solve the governing conservation equations of mass, momentum and energy using FLUENT® [19] with the segregated solver. Particle synthesis is not modeled and the entire flow field is assumed to be Ar. The 2nd order upwind scheme is used to handle convection-diffusion discretization and velocity and pressure are decoupled using the SIMPLE algorithm [20].

The solutions are considered converged when the monitored residuals of mass, velocity, and temperature are less than 10^{-4}, 10^{-4} and 10^{-8}, respectively. The model is parallized by partitioning the domain and utilizing multiple-nodes. A nonuniform and very fine grid is applied in the first 5 cm of the reactor. Grid independent solutions are obtained by dynamically adapting the grid every 200 iterations. Converged solutions are obtained with 600 iterations with a wall clock time of 24 to 72 hours on a 6-node Intel Xenon 2.33 GHz Linux platform.

TABLE 1. OPERATING CONDITIONS FOR THE THREE SIMULATED CASES

Case no.	Zn(g)/Ar (l/min)	H_2O/Ar (l/min)	Ar (l/min)	Total gas (l/min)	Nominal Inlet Temperatures (K)		
					Zn(g)/Ar (at the quench ring)	H_2O/Ar (feed tube inlet)	Ar (feed tube inlet
1	0.75	1.42	5.70	7.87	900	473*	298
2	0.75	2.84	1.42	5.01		457	
3	0.75	4.27	2.85	7.87		427	

***** All simulations are carried out using this inlet conditions

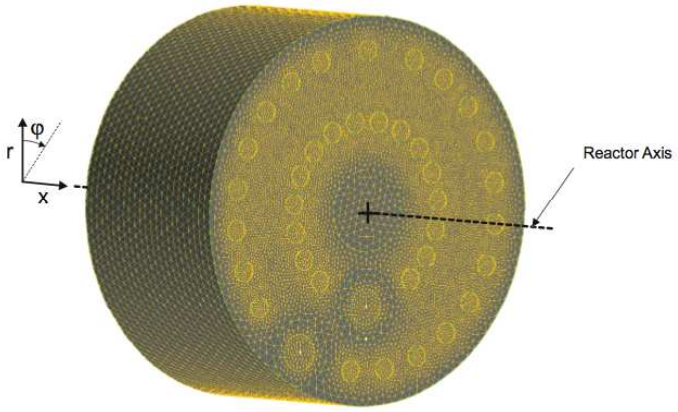

FIG. 3 QUENCH RING GRID

The model geometry construction and grid generation are carried out using GAMBIT. The computational domain is decomposed into 9 million cells with a T-Grid (Tet/Hybrid). Figure 3 shows the quench ring grid. The quench ring is located ($27 \le x \le 28$ cm) upstream of the reaction section. The upstream side of the quench ring is modeled as an isothermal surface at 843 K based on measured data. The flow of Ar at the inlet to the quench ring is 900 K. Jet impingement of the inlet flows is included in the model. The impinging flow creates a nonuniform flow among the individual outlet holes in the quench ring. The model predicts a non uniformity from the average jet velocity of ± 18 % in the inner ring of jets and ± 44 % in the outer ring of jets.

The reaction section is divided into two parts in order to specify the thermal boundary conditions. The reaction section immediately downstream of the quench ring ($28 \le x \le 38$ cm) corresponds to the section of the quartz tube that rests on the insulating mount in the furnace. Here the reactor surface is modeled as adiabatic. The reaction section ($38 \le x \le 48$ cm) is wrapped with an electrical tape heater. A uniform heat flux boundary condition is applied at the surface in this section of the reactor. The applied heat flux is 250 W/m^2.

The collection section ($48 \le x \le 65$ cm) is the stainless steel portion of the reactor. It is not insulated and thus a free convective/radiative boundary condition is applied. The emissivity of the stainless steel is assumed equal to be 0.2. All solid surfaces are no slip. Temperature dependent thermophysical properties are based on regression of tabulated data [21].

3.2 Experimental Method

Before each experiment, the masses of the filter, the glass crucible and the Zn pellets (99% purity) are recorded. The nominal weight of Zn is 0.5 gram. The experiments are initiated by purging the reactor with argon. The valves for the argon carrier gas (ultra pure) and the separate Ar flow to the quench ring are opened and the tape heater is switched on. In all experiments, the furnace set point temperature is 1023 K, yielding a Zn(g)/Ar temperature of about 900 K at the inlet of the quench ring at x = 27 cm. The H_2O/Zn molar ratio is 350. The zinc partial pressure is 9.4 mmHg. When the average reaction section wall temperature reaches 573 K (in approximately 45 minutes), the valve for the H_2O/Ar mixture is opened and the furnace heating of zinc pellets is initiated. The furnace reaches 1023 K in about 10 minutes.

The hydrogen concentration in the effluent stream is analyzed at two-minute intervals throughout the experiment. Each sample is obtained over 6 s. Hydrogen production rate is determined as

$$H_{2,\text{Production}} = \dot{V}_{H_2} \cdot \rho_{H_2} \tag{3}$$

where $\dot{V}_{H_2}$ is the volumetric flow rate of hydrogen produced during the experiment and ρ_{H_2} is the molar density. The flow of gases is terminated when the hydrogen production is less than 0.2 ml/min.

The percent conversion for each experiment is calculated according to

$$H_{2,\text{Conversion}} = \frac{V_{H_2}}{V_{Th} \cdot m_{Zn}} \text{x} 100\,, \tag{4}$$

where V_{H_2} is the volume of hydrogen produced, V_{Th} is the theoretical volume of hydrogen produced by the hydrolysis of 1 gram of Zn, and m_{Zn} is the evaporated mass of Zn. The Zn loaded into the crucible is evaporated completely during each experiment.

At the end of each experiment, flows to the quench ring are turned off with the exception of the carrier Ar, which continues to flow for 10 minutes. When the reactor is cooled to room temperature, the masses of the crucible, the filter and any loose particles in the reactor are recorded. The deposits on the wall of each section of the reactor are removed with a soft brush and their mass is also measured. The composition and the mean crystallite size of the material deposited on the quartz reactor surface and on the filter at the end of the reactor are analyzed by X-ray diffraction (Bruker-AXS D5005 Diffractometer with 2.2 kW sealed Cu Source). The size and concentration of aerosol are measured via SMPS for experiment 2.

Centerline temperatures are measured in separate experiments without Zn nanoparticles. A 0.32 cm diameter K-type stainless steel thermocouple probe is positioned axially in the reactor using a metric ruler and positioned radially using two stainless steel spacers. The spacers are positioned roughly 20 cm apart and fix the probe in the center of the reactor tube. Upstream of the quench ring, a steel radiation shield is placed around the probe tip. The shield is removed for measurements downstream of the quench ring where the probe tip is no longer exposed to the furnace radiation in order to minimize disruption of the jet flows. The centerline temperature at x = 28 cm is not measured to avoid probe contact with the quench ring. The first measurement downstream of the quench ring is taken at x = 29 cm.

Wall temperatures are measured by placing K-type thermocouples in contact with the outer surface of the 2.0 cm quartz tube. The thermocouple beads are approximately 2 mm in diameter.

4. RESULTS

4.1 Numerical

Contours of streamwise gas speed are shown in Fig. 4 in a horizontal plane at the mid point of the tubular reactor. Data are shown from x = 27 to 32 cm. The feed tubes to the quench ring are not visible in this plane. The streamwise radial velocity profiles at x = 29, 30, 32 and 48 cm are plotted in Fig. 5. A comparison of case 1, which has the highest flow rate of Ar in the outer ring of the quench device, to cases 2 and 3 demonstrates a major difference in the flow fields. In case 1, the higher speed jets of Ar near the reactor wall entrain the flows nearer the center of the reactor and the entire flow field is directed radially outward toward the wall of the quartz reactor tube over a distance of 5 cm downstream of the quench ring. This flow field is expected to result in higher deposition of nucleated Zn particles. In cases 2 and 3, the center and outer jets are entrained by the middle jet yielding an annular region of higher flow approximately 3 mm from the reactor centerline. This flow pattern is expected to decrease particle deposition relative to case 1. The velocity profiles flatten at increasing axial distance from the quench ring (Figs. 5c and d), and the confined jets merge at x = 48 cm.

Figures 6(a)-(c) show isotherms for the three cases in the same plane used to display the velocity data. In all cases, the argon carrier gas temperature decreases by 15 K within the quench ring because the quench ring is cooled by the internal impinging Ar flows. Just after the quench ring, the gas temperature decreases sharply and continues to decrease downstream more slowly. In case 1, the gas temperature drops approximately 147 K within 2 cm of the quench ring. In cases 2 and 3 the drop in temperature over the same distance is 61 and 91 K. Jet entrainment plays an important role in the transport of the thermal energy of the carrier gas to the cooler outer jet flows. The apparent asymmetry in the velocity and temperature contours is due to the presence of the feed tubes for the outer co-axial jets. The feed tubes containment within the reactor partially diminishes the effectiveness of the quench ring. The model predicts a rise of nearly 380 K in the temperature of Ar as it flows from the inlet of the feed tubes to the quench ring. Deposition of nanoparticles on the cooler feed tubes is anticipated from these results and is observed in the experiments.

4.2 Experimental

The measured gas temperatures provide an assessment of the cooling rate achieved by use of the quench ring. Figures 7(a) and (b) show the axial centerline gas temperature distribution. Numerically predicted temperatures are included for comparison. The centerline temperature distribution measured from the crucible to the end of the reactor is shown in Fig. 7(a), and an expanded plot of the temperature distribution near the quench ring ($27 \leq x \leq 30$ cm) is shown in Fig. 7(b). The measurement uncertainty is primarily due to radiation heat transfer between the reactor walls or radiation shield (depending on measurement position) and the thermocouple probe, and is estimated using the method described in [22]. Maximum uncertainty is ± 8 %, and for clarity is shown only on the data points for experiment 3 in Figs. 7(a) and 7(b).

As can be seen in Figs. 7(a) and 7(b), the predicted gas temperatures are higher than measured values. Near the quench ring at x = 29 cm, the model over predicts the gas temperature by 75 K. Further downstream between x = 32 and 50 cm the model over predicts the gas temperature by as much as 100 K. We attribute the difference between predicted and measured temperature primarily to the assumption of an adiabatic wall in the section from x = 28 to 38 cm. Despite the quantitative differences in the predicted and measured temperatures, the values agree in a relative sense. At x = 29 cm, the highest predicted and measured temperatures are for case 2 and the lowest temperatures are for case 1.

As best illustrated in Fig. 7(b), the quench ring reduces the carrier gas temperature from about 900 K at the inlet of the quencher to 705, 764, and 737 K at x = 29 cm for experiments 1, 2, and 3 respectively. These temperatures are below the zinc saturation temperatures of 741, 768, and 742 K for the three cases. Particle synthesis is possible within 1 cm of the quench ring in each case and is proven from observation of particle deposition patterns. The zinc saturation temperature is calculated as [23]

$$\log P_{Zn,S} = -20.31 - \frac{4636.2}{T_{sat}} + 10.07 \log T_{sat} - 0.0038\ T_{sat} + 4.89\times10^{-7}\ T_{sat}^{\ 2} \quad (5)$$

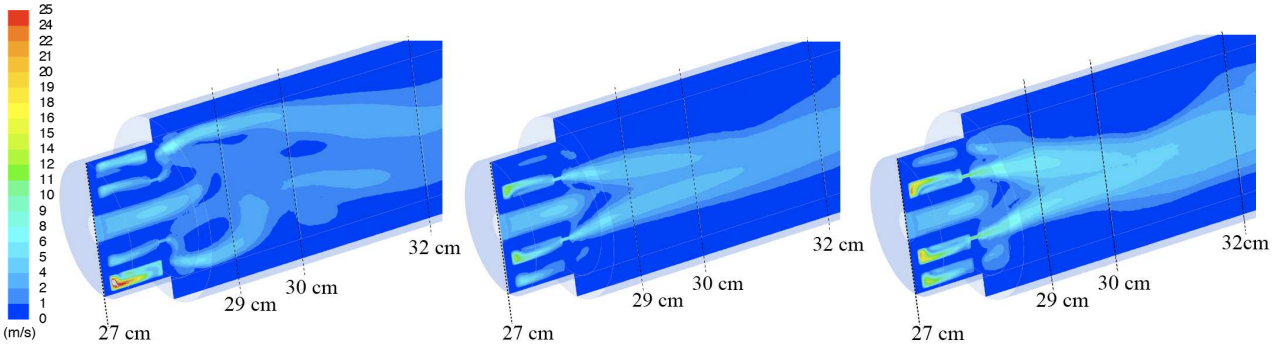

(a) **(b)** **(c)**

FIG. 4 VELOCITY ISO-CONTOURS (a) CASE 1 (b) CASE 2 (c) CASE 3

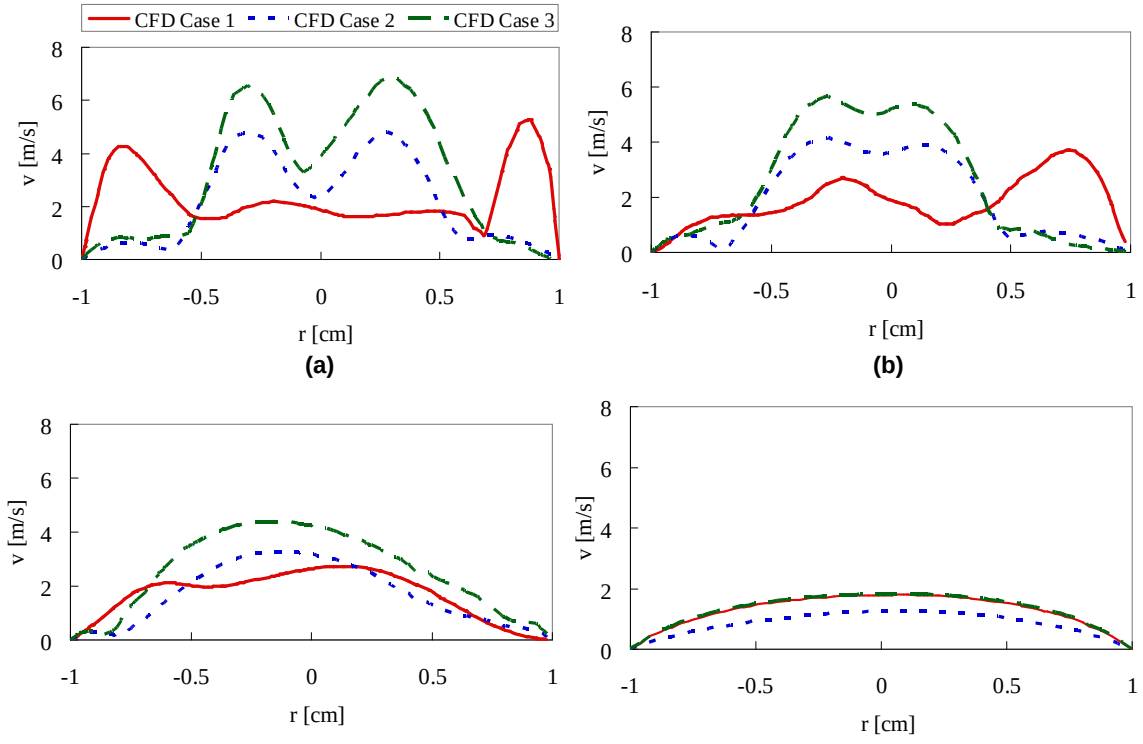

FIG. 5 VELOCITY PROFILES AT (a) x = 29 cm (b) 30 cm (c) 32 cm (d) 48 cm

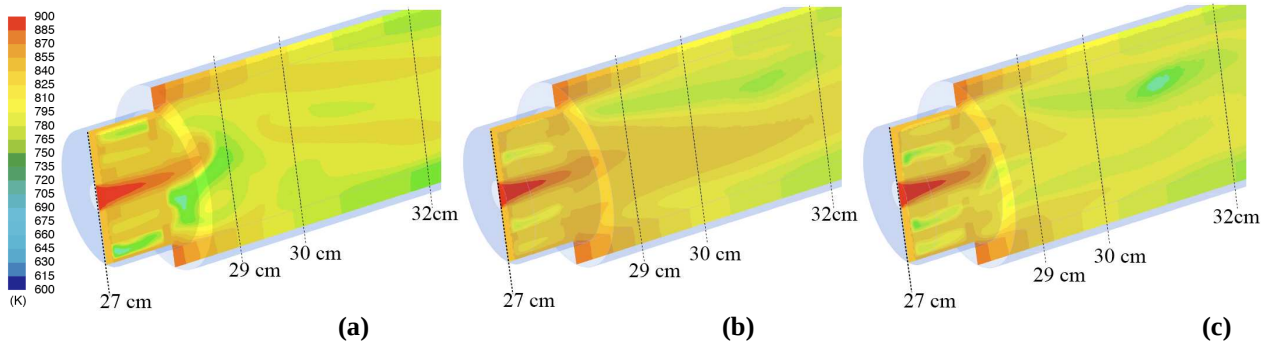

(a) **(b)** **(c)**

FIG. 6 TEMPERATURE ISO-CONTOURS (a) CASE 1 (b) CASE 2 (c) CASE 3

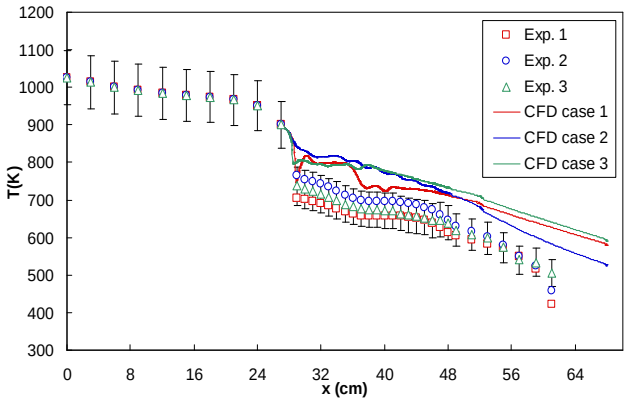

(a)

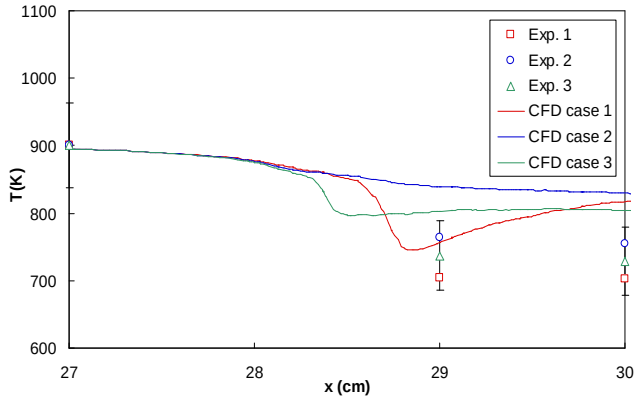

(b)

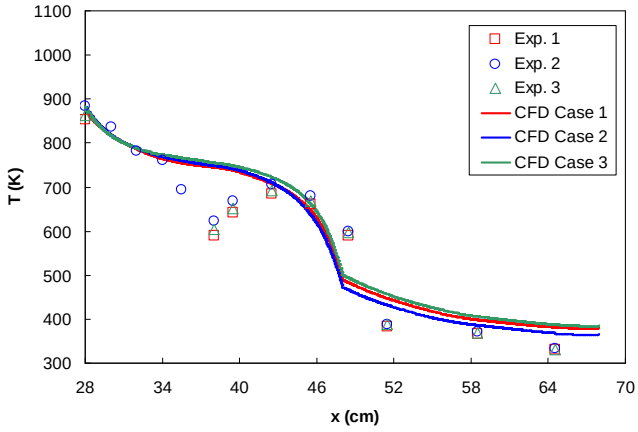

(c)

FIG. 7 PREDICTED AND MEASURED (a), (b) CENTERLINE GAS and (c) WALL TEMPERATURES

The saturation pressure, $P_{Zn,S}$, is determined from the mole fraction of the zinc using the evaporated mass of zinc and the measured mass flow rates of argon and steam. Experimental quench rates cannot be accurately estimated from the gas temperatures measured downstream of the quench ring because the first downstream measurement at x = 29 cm is below the saturation temperature of Zn. Quench rates predicted from the numerical data shown in Fig. 7(b) are estimated as

$$\frac{\Delta T}{\Delta t} = \frac{(T_{x=27cm} - T_{sat})}{(x_{sat} - x_{27})} \overline{U}_{x_{sat}} \qquad (6)$$

where $\overline{U}$ is the average velocity at x_{sat}. The model predicts the gas cools to the Zn saturation temperature at x = 37.0, 41.4 and 46.4 cm for cases 1, 2, and 3. The corresponding predicted quench rates are 1759, 728 and 873 K/s. Despite the rapid quench to temperatures below the zinc saturation temperature in the first few centimeters downstream of the quench ring, centerline gas temperatures are held between 630 and 730 K in the reaction section from x = 30 to 48 cm because the reactor wall is heated between x = 38 and 48 cm.

The measured and predicted wall temperatures are plotted in Fig. 7(c) along the reaction and collection sections. Measured surface temperature decreases from 854, 883 and 862 K at x = 28 cm to 590, 623 and 604 K at x = 38 cm for experiments 1, 2 and 3. The predicted wall temperatures are about 100 K higher at x = 38 cm. This difference is attributed to the modeling assumption of an adiabatic boundary along the insulated support. Measured wall temperatures rise in the section wrapped with an electrical tape heater. Predicted temperatures at 42 cm are 685, 706, and 692 K for experiments 1, 2 and 3. Predicted temperatures are within 60 K of the measured values. In the collection section ($48 \leq x \leq 65$ cm), the measured temperatures drop from about 600 at x = 48 cm to 330 K at x = 65 cm. Measured and predicted temperatures in this region are within 25 K of each other.

The synthesis and hydrolysis of Zn nanoparticles are characterized from in-situ particle measurements via nano-SMPS and XRD analysis of the particles collected on the filter and from the walls of the reactor. Centerline aerosol concentration at x = 48 cm is 10^8 particles/cm^3 with a mean particle size of 16 nm. In all experiments, particles are present on the reactor surface. The particles are loose and are easily removed with a soft brush. The poor adhesion to the wall suggests particle deposition rather than vapor deposition.

The color of the deposited particles and XRD measurements indicate the extent of their reaction. The particles vary in color from white and light gray (ZnO) near the quench ring to black (Zn) near the end of the reactor where temperatures are too low for hydrolysis. Figure 8 shows the XRD analysis of the composition of the material removed from the wall as a function of distance from the quench ring for each experiment. The decreasing ZnO content along the length of the reactor is consistent with the color of the deposits and the decrease in wall and gas temperatures. There is a slight increase in the percentage of ZnO at x = 40 cm due to the increase of wall temperature at that position (see Fig. 7(c)). The size of the particles removed from the reactor wall at $28 \leq x \leq 48$ cm is 33 to 55 nm for the ZnO and 38 to 68 nm for the Zn.

Fewer and slightly smaller particles are collected on the filter. Particles collected on the filter represent 9, 9 and 12 % of the evaporated zinc containing 22, 24, and 34 % ZnO for experiments 1, 2, and 3, respectively. Average particle size determined by XRD is 22 to 33 nm for the ZnO and 39 to 50 nm for the Zn. The fact that ZnO particles are smaller than Zn

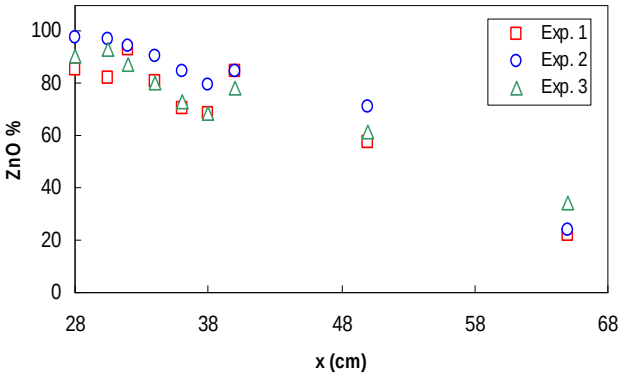

FIG. 8 COMPOSITION OF PARTICLES

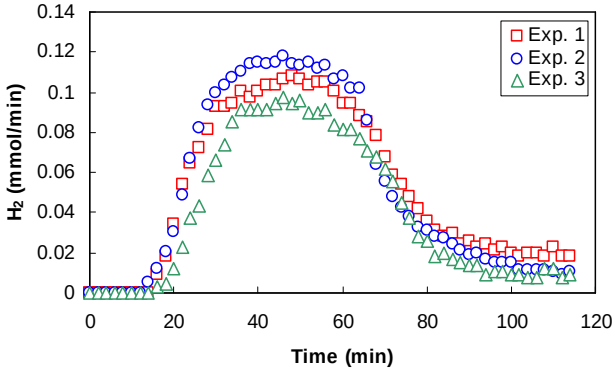

FIG. 9 HYDROGEN PRODUCTION RATE (mmol/min).

particles is consistent with data of Ernst *et al.* [12] and Muller *et al.* [24]. Similar observations of deposited particle ZnO content are made by Funke *et al.* [15]. They also note that the particles collected on the filter were only partially hydrolyzed while the particles deposited on the hot reactor wall were completely hydrolyzed.

Hydrogen production rates (mmol/min) are plotted in Fig. 9. On this plot, t = 0 min represents the time when H_2O/Ar is introduced to the reactor and the electric furnace is turned on. The furnace reaches 1023 K at t = 10 min. The first hydrogen is detected at t = 16 min. Hydrogen production rate increases until t = 36 min. The increase in the hydrogen production from t = 16 to t = 36 min is attributed to the initial increase in evaporation rate. Ernst *et al.* [13] found that the zinc evaporation rate requires nearly 12 to 15 minutes to reach steady state. Hydrogen production remains nearly constant from 36 to 60 minutes when the Zn is completely evaporated (confirmed by visual observation). From t = 0 to 60 min, the amount of hydrogen produced is 65, 71, and 68 % of the total for experiments 1, 2, and 3 respectively. The decrease in hydrogen production rate after 60 minutes is attributed to a reduced rate of hydrolysis as particles deposited on the wall continue to hydrolyze. Once a ZnO layer is formed, the hydrolysis reaction is limited by the diffusion of the reactants through the layer [9]. After 90 minutes, hydrogen production continues to decrease but at a slower rate. This result is consistent with an increase in the diffusion time through a growing oxide layer and slower hydrolysis of the zinc in the cooler collection section. The total hydrogen conversions for experiments 1, 2, and 3 are 79, 79, and 61 %, respectively. These values are lower than those obtained in prior experiments at temperatures above the Zn saturation temperature [8-10,12]. Above the saturation temperature, zinc vapor and steam react heterogeneously at the hot walls of the reactor. In the present experiments, the Zn particles entrained in the gas and the particles deposited on the wall react with steam in the reaction section.

A comparison of both particle deposition and hydrogen conversion in the three experiments elucidates the hydrolysis process. The lowest hydrogen conversion (61 %) is produced in experiment 3. This experiment yields the greatest mass of particles at the filter and in the collection section (16.1% of the evaporated zinc) where temperatures are less than 600 K. Particles in the cooler collection section of the reactor react slower than those deposited in the hotter reaction section.

Hydrogen conversion in experiments 1 and 2 is 79%. In both of these experiments, more particles remain in the hotter reaction section than in experiment 3. Only 11% of the evaporated zinc is recovered from the collection section and on the filter. In experiment 1, the particles are forced toward the wall near the quench ring, as predicted by the model. In experiment 2, the total flow rate is lowest providing a longer gas residence time from the quench ring to the filter (0.42 as opposed to 0.23 and 0.26 s for experiments 1 and 2). Thus for different reasons, particles remain in the hotter reactor section longer and react faster than in experiment 3. The presence of non attached (loose) particles and the relative ease with which particles are removed from the wall precludes vapor deposition. Hydrolysis occurred primarily in the region near the quench ring where temperatures are above ~650 K and the mass of deposited particles is highest.

5. CONCLUSION

Hydrolysis of zinc nanoparticles as the second step in a solar thermochemical water splitting cycle has been studied in a tubular reactor. A key component of the reactor is a quencher that rapidly cools a mixture of zinc(g), argon and steam with three co-axial and multi-inlet confined jets. In the quencher, the center jet is Zn(g) in an argon carrier gas, the surrounding jet is an H_2O/Ar mixture, and the outer jet is argon. Three-dimensional modeling of the flow and temperature fields in the quench ring and the reactor show that the relative jet velocities control the degree of mixing and structure of the flow field. The center jet of Zn(g) is rapidly entrained and quenched by the faster outer jets. When the Ar jet near the wall is fastest, the Zn particle laden flow in the core is forced radially outward towards the wall. Whereas, when the middle H_2O/Ar jet is fastest, the Zn particle laden flow remains in the center of the tubular reactor.

The present experiments reveal competing effects of increasing quench rates. To achieve high quench rates and thus more and smaller nanoparticles, the flow of Ar/steam must be increased. An increase in coolant flow rate, however, reduces the residence time in the reaction section for particles that remain in the flow field. In-flight residence times longer than those in the present reactor (on the order of 0.5 s) are required for full conversion of the Zn aerosol. The present study, as well as prior studies demonstrate, the difficulty of preventing nanoparticle deposition on the reactor surfaces.

Continuous recovery of the nanoparticles has not yet been accomplished. On the other hand, deposition of particles on the wall of the reactor where temperatures are above about 650 K yields higher hydrogen conversions that does hydrolysis of gas borne zinc nanoparticles at the residence times studied to date.

ACKNOWLEDGEMENT

The project is funded by the University of Minnesota Initiative for Renewable Energy and the Environment. The University of Minnesota Supercomputing Institute provided computational resources. Parts of this work were carried out in the Institute of Technology Characterization Facility, University of Minnesota, which receives partial support from NSF. We thank Professor Aldo Steinfeld at Swiss Federal Institute of Technology (ETH-Zurich) for his collaboration and financial support of the Master thesis of Marc Brülhart.

REFERENCES

[1] Steinfeld, A., 2002, "Solar Hydrogen Production via A Two-Step Water-Splitting Thermochemical Cycle Based on Zn/ZnO Redox Reactions," International Journal of Hydrogen Energy, 27, pp. 611-619.

[2] Steinfeld, A., 2005, "Solar Thermochemical Production of Hydrogen—a Review," Solar Energy, 78, pp. 603-615.

[3] Palumbo, R., Lédé, J., Boutin, O., Elorza Ricart, E., Steinfeld, A., Moeller, S., Weidenkaff, A., Fletcher, EA., and Bielicki, J., 1998, "The Production of Zn From ZnO in A Single Step High Temperature Solar Decomposition Process," Chemical Engineering Science, 53, pp. 2503-2518.

[4] Haueter, P., Moeller, S., Palumbo, R., and Steinfeld, A., 1999, "The Production of Zinc by Thermal Dissociation of Zinc Oxide – Solar Chemical Reactor Design," Solar Energy, 67, pp.161-167.

[5] Moeller, S., and Palumbo, R., 2001, "The Development of A Solar Chemical Reactor for the Direct Thermal Dissociation of Zinc Oxide," Journal of Solar Energy Engineering, 123, pp. 83-90.

[6] Schunk, L. O., Haeberling, P., Wepf, S., Wuillemin. D., Meier, A., and Steinfeld, A., 2007, "A Rotary Receiver-Reactor for the Solar Thermal Dissociation of Zinc Oxide," Proceedings of the ASME Energy Sustainability Conference, Paper No. 36078, Long Beach, CA, June 27-30.

[7] Perkins, C., Lichty, P., and Weimer A. W., 2007, "Determination of Aerosol Kinetics of Thermal ZnO Dissociation by Thermogravimetry," Chemical Engineering Science, 62, pp. 5952-5962.

[8] Wegner, A., K., Ly, H.C., Weiss, R.J., Pratsinis, S.E. and Steinfeld, A., 2006, "In Situ Formation and Hydrolysis of Zn Nanoparticles for H_2 Production by the 2-Step ZnO/Zn Water-Splitting Thermochemical Cycle," International Journal of Hydrogen Energy, 31, pp. 55–61.

[9] Weiss, R. J., Ly, H. C., Wegner, K., Pratsinis, S. E., and Steinfeld, A., 2005, "H_2 Production by Zn Hydrolysis in A Hot-Wall Aerosol Reactor," American Institute of Chemical Engineers Journal, 51, pp. 1966 -1970.

[10] Abu Hamed, T., Davidson, J.H., Stolzenburg, M., 2007, "Hydrogen Production via Hydrolysis of Zn in A Hot Wall Flow Reactor," Proceedings of the ASME Energy Sustainability Conference, Paper No. 36176, Long Beach, CA, June 27-30. To appear in the Journal of Solar Energy Engineering, November 2008.

[11] Abu Hamed, T., Davidson, J.H., Haltiwanger, J.F., 2007, "Hydrogen Production via Hydrolysis of Zinc Nanoparticles" Proceedings of the AICHE Annual Meeting, Salt Lake City, Utah, November 4 -9.

[12] Ernst, F.O., 2007, "Cosynthesis of H_2 and Nanocrystalline ZnO Particles by Zn Aerosol Formation and In-situ Hydrolysis," Ph.D. Dissertation No. 17272, ETH-Zurich, Zurich, Switzerland.

[13] Ernst, F. O., Tricoli, A., Pratsinis, S. E., and Steinfeld, A., 2006, "Co-Synthesis of H_2 and ZnO by In-Situ Zn Aerosol Formation and Hydrolysis," American Institute of Chemical Engineers Journal, 52(9), pp. 3297-3303.

[14] Piatkowski, N., 2007, "Zn-nanoparticle in-situ Hydrolysis for Hydrogen Production in a High Quench Rate Reactor," Master Thesis, ETH-Zurich, Zurich, Switzerland.

[15] Funke, H.H., Diaz, H., Liang, X., Carney, C.S., Weimer, A.W., and Li, P., 2008, "Hydrogen Generation by Hydrolysis of Zinc Powder Aerosol," International Journal of Hydrogen Energy, 33 (4), pp. 1127-1134.

[16] Panda, S., Pratsinis, SE., 1995, "Modeling the Synthesis of Aluminum Particles by Evaporation– Condensation in an Aerosol Flow Reactor,". Nanostructured Materials, 5, pp. 755-767.

[17] Woodfield, P.L., 2003 "Numerical Study of Enhancement of Laminar Flow Mixing using Multiple Confined Jets in a Micro-can Combustor," International Journal of Heat and Mass Transfer, 46, pp. 2655-2663.

[18] Jahnke, S., Kornev, N., Tkatchenko, Hassel, E., and Leder, A., 2005, "Numerical Study of Influence of Different Parameters on Mixing in a Coaxial Jet Mixer using LES," Heat and Mass Transfer, 41, pp. 471-481

[19] Fluent 6.2. User's Guide, 2005, Lebanon. NH, USA

[20] Patankar, S.V., 1980, Numerical Heat Transfer and Fluid Flow, Hemisphere Pub. Corp., New York.

[21] Rabinovich, V.A., 1988, Thermophysical Properties of Neon, Argon, Krypton, and Xenon, Hemisphere Pub. Corp., New York.

[22] Figliola, R.S., Beasley, D.E., 2006, Theory and Design for Mechanical Measurements. 4th ed. John Wiley & Sons, Inc.

[23] Yaws, C. L., 1999, Chemical Properties Handbook. New York, NY: McGraw-Hill.

[24] Müller, R., and Steinfeld, A., 2008, "H_2O-Splitting Thermochemical Cycle Based on ZnO/Zn-Redox: Quenching the Effluents from the ZnO Dissociation," Chemical Engineering Science, 63(1), pp. 217-227.